Article:

Ho, VL, Dorrell, RM orcid.org/0000-0003-4257-7273, Keevil, GM et al. (2 more authors) (2018) Pulse propagation in turbidity currents. Sedimentology, 65 (2). pp. 620-637. ISSN 0037-0746

https://doi.org/10.1111/sed.12397

Pulse propagation in turbidity currents

Ho V. Luan[1*], Dorrell R.M.[1], Keevil G.M.[1], Burns A.D.[2] and McCaffrey W.D.[1]

1. School of Earth and Environment, University of Leeds, Leeds, LS2 9JT, UK.

2. School of Chemical and Process Engineering, University of Leeds, Leeds, LS2 9JT, UK.

*Corresponding author: eevlh@leeds.ac.uk

ABSTRACT

Submarine turbidity currents are a key mechanism in the transportation of clastic sediments to deep seas. Such currents may initiate with a complex longitudinal flow structure comprising flow pulses (e.g. by being sourced from retrogressive sea floor slope failures) or acquire such structure during runout (e.g. following flow combination downstream of confluences). A key question is how far along channel pathway complex flow structure is preserved within turbidity currents as they run out and thus if flow initiation mechanism and proximity to source may be inferred from the vertical structure of their deposits. To address this question, physical modelling of saline flows has been conducted to investigate the dynamics of single-pulsed vs. multi-pulsed density driven currents. The data suggest that under most circumstances individual pulses within a multi-pulsed flow must merge. Therefore initiation signatures will only be preserved in deposits upstream of the merging point, and may be distorted approaching it; downstream of the merging point, all initiation signals will be lost. This new understanding of merging phenomenon within multi-pulsed gravity currents broadens our ability to interpret multi-pulsed turbidites.

Keywords: turbidity currents, multi-pulsed turbidity currents, seismo-turbidites, pulsed turbidites, stacked turbidites, signal shredding.

1. INTRODUCTION

Gravity currents are driven by a density difference between two fluids, and are widespread in both industrial scenarios and natural settings. Turbidity currents are a form of dilute particulate gravity flow in which the flows move under the gravitational action upon dispersed sediments suspended within the interstitial fluid (Middleton, 1993; Huppert, 1998; Kneller & Buckee, 2000; Sequeiros, 2012). Turbidity currents in natural settings can range up to hundreds of meter in thickness (Piper *et al*., 1988; Sumner & Paull, 2014) with durations that may extend up to hours or days (Piper *et al*., 1999; Xu *et al*., 2004; Mikada *et al*., 2006); they are a principal mechanism by which sediment is transported from continents to deep seas (e.g. Simpson, 1982; Talling *et al*., 2015). Turbidity currents can be initiated by submarine slope failures (triggered by earthquakes or other mechanisms) or by direct hyperpycnal underflow into the oceans; they commonly flow through submarine channels into the deep oceans (Mulder & Alexander, 2001; Best, *et* al, 2005; Piper & Normark, 2009).

Sediments deposited by turbidity currents – turbidites - commonly exhibit continuously upward fining of mean grainsize (Fig. 1). This is referred to as "normal grading" (Bouma, 1962; Lowe, 1982; Gutiérrez-Pastor *et al*., 2013). However, it is not uncommon for turbidites to show more complex grading profiles, such as inverse grading (e.g. Kneller and McCaffrey, 2003; Mulder *et al*., 2003). On the basis that the grain size at any particular level in a deposit relates to the instantaneous basal shear stresses, normal grading suggests deposition from a waning flow, whereas, inversely graded (upward coarsening) deposits suggest deposition from waxing flow (Kneller & Branney, 1995; Kneller & McCaffrey, 2003; Mulder *et al*., 2003; Amy *et al.*, 2005; Basilici *et al.*, 2012, cf. Hand, 1997). A more complex exception from normal grading patterns is seen when repeated intervals of coarsening are seen superimposed upon an overall normally-grading profile. Beds exhibiting this pattern are here described as a "pulsed" or "multi-pulsed" turbidites, as the implication is that pulses of increased velocity occurred in the overpassing flow at the point of deposition. Pulsed turbidites can be differentiated from "stacked" turbidites which, although superficially similar, represent the closely vertically juxtaposed deposits of two or more individual turbidity currents; in practice, distinguishing the two can be challenging where later flows erode into the deposits of earlier flows to produce deposit amalgamation and intervening fine grained material is absent. When submarine turbidites show deviations from a continuous normal grading, a variety of mechanisms can be invoked to explain pulsed flow generation, for example discrete episodes of retrogressive slumping (Piper *et al*., 1999; Canals *et al*., 2004; Bull *et al*., 2009), variations in ground shaking in currents initiated by single seismic events (Goldfinger *et al*., 2012), variations in the flood hydrograph for hyperpycnally generated flows (Mulder & Alexander, 2001) and flow combination along the pathway of channel confluences (Nakajima & Kanai, 2000; Ismail, *et al*., 2016). In addition flow reflection in confined settings has also been invoked to cause pulsing (e.g. Haughton, 1994). Research on how these mechanisms might be distinguished in the depositional record of pulsing flows is less extensive (see examples in Goldfinger *et al*., 2012). A key consideration in this regard is how long non-monotonic variations in mean flow velocity along the flow may persist from source, and thus potentially be indicative of the flow generation mechanism; a related consideration is whether the degree to which a deposit approaches a normal grading profile may be an indirect indicator of distance from source.

Here, saline flow experiments are reported with the aim of informing understanding of the dynamics and evolution of pulsed turbidity currents, and exploring the possible implications for the interpretation of vertical depositional grading profiles. A principal goal is to review and extend the inferences regarding flow behaviour and proximity to source that can reasonably be made in natural turbidites. This contribution: i) presents novel experimental data that detail the variation of multi-pulsed flow dynamics; ii) assesses how flow dynamics may be interpreted from turbidite grading structure, and iii) reviews two case studies in the which the interpretational template of turbidites with complex grading profiles is reviewed and broadened.

2. METHODOLOGY

2.1. Experimental set-up and research methodology

The methodology of generating gravity currents in lock exchange flumes has been widely applied by various authors (e.g. Middleton, 1966; Holyer & Huppert, 1980; Britter & Simpson, 1981; Lowe *et al*., 2002; Gladstone *et al*., 2004). In the work described here, lock exchange experiments of saline flows were conducted in order to gain an understanding of the internal dynamical structure of turbidity currents. Although they do not take into account the effects of particle transport, as occurs in natural turbidity currents, saline flows are a well-established proxy for studying such flows (e.g. Kneller and Buckee, 2000; Islam and Imran, 2010; Hogg *et al.,* 2016). Similarly, turbulent laboratory-scale flows are thought to deliver a good representation of the dynamics of flow at natural scale (e.g. Paola *et al*., 2009). Figure 2 shows the experimental set-up, in which a 5 m long Perspex flume with multiple lock-exchange gates was used, incorporating overspill boxes at both ends to reduce the effect of waves caused by the removal of the lock gates. Two 12.5 cm-long lock boxes were set up in series at one end to enable the generation of multi-pulsed flows, using saline fluid with 5% density excess (1050 kgm^{-3}) as a proxy for turbidity currents. Using a pneumatic lock-gate driver, the upstroke speed of each lock gate was set at 1.0 ms^{-1} so that any resulting turbulence was minimized, without being so slow that a partially-withdrawn lock gate affected the counter flow of fluid into the lock. The release time delay of the second gate could be adjusted to within 1/10 s of the first release; here it was set to 4 s so that the interaction between pulses in a bi-pulsed flow occurred within the length of the flume. To model single-pulsed flows, the delay was set to zero. The dense saline fluid was prepared in a 180 l mixer, and monitored to ensure consistent density. It was pumped slowly into the lock boxes via an intake valve on the bottom of each lock box, displacing fresh water above whilst preserving a sharp upper boundary. Each lock box was filled to a depth of 0.05 m with dense fluid dyed yellow in the first box and blue in the second to enhance flow visualization and front position tracking. The total lock box depth equalled the 0.25 m depth of the external ambient. The 1:5 depth ratio maintains fully turbulent, subcritical flow (Reynolds numbers were c. 2,000 and Froude numbers less than 1) while allowing suitable depth scaling approximating to real-world submarine flow, where flow to ambient depth ratios are 1:8 or greater (Piper *et al*., 1988; Xu *et al*., 2004).

Five HD interlinked cameras were deployed to capture a wide range of view of the flume. The cameras were carefully aligned so as to prevent image distortions and stitching artefacts. VirtualDub and Avisynth were used to stitch five linked video tracks together, based on an audio time cue; camera synchronization was within 1 frame (0.042 s). The alignment of the five cameras was checked using gridlines on the bottom of the flume (Fig. 3). The method of profiling Acoustic Doppler Velocimetry (ADV) was used to measure spatio-temporal variation of horizontal streamwise velocities (Craig *et al*., 2011; MacVicar *et al.,* 2014; Brand *et al*., 2016). This methodology offers velocity profile measurements at high frequencies and with high resolution. The ADV probe head was positioned 7.1 cm above the bed of the flume at 13 different locations along the flume (Fig. 2), capturing a measurement of 30 mm flow depth at each position. Both the dense fluid and the ambient were seeded with neutrally-buoyant particles of 10 µm diameter to generate a consistent acoustic reflection. Spatio-temporal depth-averaged velocity profiles were constructed for both single and multi-pulsed flows using the following equation:

$$\bar{u} = \frac{\int_0^h v\, dz}{h}$$

where v is the instantaneous velocity of the flow and $h = 0.03\ m$.

2.2. Dynamics of density currents

The dynamics of lock-gate release density currents can usefully be associated with the slumping, inertial and viscous flow regimes of flow evolution, varying in each due to the changing relative significance of buoyancy, inertial and viscous forces (Huppert & Simpson, 1980; Huppert, 1982; Rottman & Simpson, 1983; Bonnecaze *et al*., 1993; Kneller *et al*., 1999; Amy *et al*., 2005; Di Federico *et al*., 2006; Huppert, 2006; Sher & Woods, 2015). The slumping phase can extend up to 10 lock lengths from the initiation point; during this phase the gravity current is driven mainly by buoyancy forces resulting from the density difference between the dense fluid and the ambient. The buoyancy force of the flow is balanced by frictional forces, principally caused by the return flow of ambient fluid balancing the slumping of dense fluid out of the lock box; the flow travels with nearly constant velocity in the slumping phase. During the inertial phase, inertial effects become important; this regime is characterized by flow deceleration. Once the flow becomes sufficiently shallow, frictional forces exceed buoyancy and inertial forces, and the flow enters the viscous phase, in which it continues to decelerate.

3. RESULTS

Below, the results from the single- then multi-pulsed flows are described in sequence, considering firstly the flow visualization data and then the flow velocity data.

3.1 Single-pulsed flow

To distinguish the frontal and rearward components of the single-pulsed flow, the denser than ambient fluid in the front lock box was dyed yellow, and that in the rear blue, as shown in Fig. 3A. As noted above, a zero second delay time between two lock gates enabled the instantaneous trigger of the gates and the generation of a single release of the dense fluid. Following the release, the dense fluid in the lock boxes collapsed, forming a negatively buoyant density driven flow that propagated along the bottom of the flume. As the current advanced along the flume, the blue portion of dense fluid comprising the rear 50% of the flow at initiation was advected towards the front of the current (Fig. 3A, t=2-4 s; cf. Sher & Woods, 2015). The advection formed a visible intrusion around half of the flow depth, similar to advection in Poiseuille flow (Lowe *et al*., 2002; Sher & Woods, 2015). The dyed components of the flow are inferred to have progressively mixed, changing the flow colour from yellow/blue to green. In addition, the variation in the degree of mixing between the dense fluid and the ambient is qualitatively indicated by the change in relative colour intensity of the green fluid (Fig. 3A, t=2-18 s). This change is especially pronounced at the flow head, where turbulent mixing processes are largest, due to shear-driven generation of Kelvin-Helmholtz billows (Britter & Simpson, 1978; Johnson & Hogg, 2013).

The tracking of flow front positions using video data and the collection of velocity time series using fixed instrumentation at different downstream locations permit velocity profiles of both single- and multi-pulsed flows to be detailed (Figs. 4, 5 and 6). By tracking the positions of the front (yellow) and rear (blue) components of the single-pulsed flow, two dynamical flow regimes can be identified. In the initial slumping phase, the flow advanced at a nearly constant velocity of c. 0.082 ms^{-1} for 1.25 m (c. 5 lock lengths). During the succeeding inertial phase, the flow decelerated from 0.082 ms^{-1} to 0.008 ms^{-1} s over 2 m. The viscous phase of the flow was not observed in the length of the flume covered by the cameras. The rearward portion of the single-pulsed flow was advected forwards within the flow at a nearly constant velocity of 0.1 ms^{-1}, i.e., 25% faster than the flow head, reaching the flow front during the slumping phase some 0.8 m from source (Fig. 4A). The single-pulsed flow (Fig. 5A) displayed the rapidly waxing and progressively waning velocity structure which is usually observed in lock-gate release experiments (e.g. Simpson, 1982; Kneller *et al*., 1999). The velocity maximum was located at c. 25% of the local flow depth, as commonly seen in laboratory experiments, field data and theoretical models (e.g. Kneller & Buckee, 2000; Talling *et al*., 2015). The magnitude of flow velocity was observed to decrease with increasing time and distance from source, as indicated by the change in colour intensity in Fig. 5A. The depth of the flow may be estimated by using the vertical velocity profile to establish the height of the zero velocity contour that separates downstream from upstream (return) flow (Dorrell *et al*., 2016); e.g. in Fig. 5A at 0.365m downstream position and 2.5s, h=0.015m. The spatio-temporal variation of depth-averaged velocity for single-pulsed flow is shown in Fig. 6A in which the boundary of the black region indicates the arrival of the flow in time and space. The plot shows a model of standard flow evolution in which the head velocity, indicated by the yellow to orange regions behind the black edge, is constantly high within slumping phase (up to the distance of about 1.4 m in Fig. 6A) and then decreases with increasing time and distance.

3.2. Multi-pulsed flow

Initially, a single flow pulse dyed yellow was released from the front lock box and propagated along the flume in the form of a negatively-buoyant density current (Fig. 3B, t=2 s). The second pulse was triggered 4 s after the first one, at which time the fluid comprising the initial release had collapsed to approximately one fourth of its initial depth in the front lock box (Fig. 3B, t=4 s). The second pulse was quickly advected towards the front of the flow, in the form of a visible intrusion with sharp boundaries, at approximately half of the height of the first pulse (Fig. 3B, inset t=11 s). The colour change from yellow and blue to green reflects the progressive mixing between the two pulses (Fig 3B, t=11-18 s). Eventually, the two pulses merged at a distance 1.4 m from source and the whole flow evolved in a manner similar to that of a single-pulsed flow during its inertial phase (Figs. 3 and 4). Kelvin-Helmholtz billows were generated on the back of the flow head, enhancing turbulent mixing in the flow and between the dense and ambient fluid (Britter & Simpson, 1978; Johnson & Hogg, 2013). Thus the colour shift at the flow head, as indicated by the variation in colour intensity of the green (mixed) fluid, was intensified (Fig. 3B, t=2-18 s).

Front position tracking and the collection of velocity time series enabled velocity profiles of the multi-pulsed flows to be detailed (Figs. 5 and 6). The first pulse entered its slumping phase at initiation, and had travelled at a nearly constant velocity of 0.079 ms^{-1} for 0.65 m, (approximately five 12.5 cm lock lengths) before the second pulse was released. The second pulse was released 4 s after the first (Figs. 4B and 5B) and progressively intruded into it. The combined flow accelerated at the point when the intrusion reached the flow head (Fig. 4B, inset) advancing at a nearly constant velocity of c. 0.074 ms^{-1} for 0.25 m from the point of merging. Thus, the slumping phase of the multi-pulsed flow lasted over 1.40 m (approximately six 25.0 cm lock lengths). The slumping phase ended at 1.65 m from source. The velocity of the second pulse averaged nearly 0.110 ms^{-1}, which is approximately 35% greater than the initial head velocity of the first pulse. The inertial phase of the merged multi-pulsed flow was characterized by a reduction in velocity to 0.012 ms^{-1} over a distance of about 1.85 m between 1.65 m to 3.5 m from source (Fig. 4B). As with the single-pulsed flow experiments, the viscous phase of the multi-pulsed flow was not captured within the camera range of these experiments. The multi-pulsed flow displayed a more complex velocity structure than the generic waxing-waning velocity profile observed in lock-release single-pulsed gravity currents (Fig. 5B). Two separate pulses of relatively high velocity (>0.1 ms^{-1}) were distinctly observed proximally to source (Fig. 5B, 0.365 m). The time separation between two pulses decreased as the second pulse was progressively advected towards the front of the first pulse (e.g. Fig. 5B, 0.365 m, 0.675 m and 0.865 m). At the point of merging, the two pulses tended to have similar velocities. Beyond the point of merging, the merged flow exhibited essentially the same waxing-waning velocity structure as observed in the single-pulsed flow experiments (Fig. 5A-B, 1.265 m, 1.665 m). The velocity maximum was also located at about 20% of the flow depth, as observed in the single-pulsed flow experiments. In order to visualize the spatio-temporal variation in the velocity profile of the multi-pulsed flow, a contour plot showing the depth-averaged velocity of the flow was constructed (Fig. 6B). The depth-averaged velocity of the first pulse was relatively high proximal to source (0.1 ms^{-1}). The high intensity region surrounding the dotted line on Fig. 6B indicates the signal of the advection of the second pulse within the first pulse. The initial relative timing of this signal was distorted by being progressively reduced towards the point of merging. Beyond this point, the signal of the second pulse intrusion in the velocity profile was completely lost (i.e., ''shredded'', *sensu* Jerolmack & Paola, 2010; Figs. 5B and 6B).

3.3. Single-pulsed vs. multi-pulsed flows

Multi-pulsed flow evolution is characterized by interaction of the separate pulses which eventually merge at some distance from source; such flows exhibit a pulsing character up to the point of merging. This pulsing characteristic is not seen in single-pulsed density currents. Figure 7A shows raw (unfiltered) data detailing the temporal variation of depth-averaged velocities of the single- vs. multi-pulsed flows, shown proximally to source, at the point of merging and distally from source. The surface waves set up at flow initiation were not completely removed by the overspill boxes, and resulted in a fluctuation in the raw data; the magnitudes of the fluctuations are relatively small compared to the front velocity of the flows, and are not thought to have significantly influenced the flow dynamics. To more clearly assess the flow dynamics, the raw velocity data are filtered and replotted in Fig. 7B. Before the point of merging, the depth averaged velocity profile of single-pulsed flows exhibited a standard waxing-waning velocity structure whereas the profile of multi-pulsed flows has two pronounced pulses (0-7 s at 0.365 m Fig. 7B). The time delay measured between the two velocity pulses depends on initial lag time at initiation, and also upon the point of measurement. Up to the point of merging, the time separation between the two pulses in multi-pulsed flows progressively decreased. For the multi-pulsed flow, after the peak of the second pulse passed the position of profiling, the velocity magnitude of the flow became comparable to that of a single-pulsed flow comprising the same initial dense fluid. In distal regions, both single- and multi-pulsed flows showed similar velocity structures to the normal waxing-waning velocity profile (Fig. 7B).

4. DISCUSSION

4.1. Multi-pulsed turbidity current propagation

Turbidity currents commonly develop vertical density stratification during runout, due to the entrainment of ambient fluid (Britter & Simpson, 1978; Hallworth *et al*., 1996), particle settlement (Baas *et al*., 2005) and also due to recirculation of fluid from the body into the head, where it is mixed and ejected backwards (Lowe *et al*., 2002; Sher & Woods, 2015; Hughes, 2016). It is inferred that both the single-pulsed density currents and the first pulse of multi-pulsed flows developed vertical density stratification; the change within the first pulse from an initial vertically homogeneous density profile to a stratified one can be seen from the development of a green to yellow vertical transition in the single-pulsed flow (Fig. 3A) and in the upward-lightening yellow colour intensity in the multi-pulsed flow (Fig. 3B). Consequently the second pulse intruded into the first at a neutrally buoyant level and was advected within it.

In gravity currents the velocity maximum is usually at approximately one quarter of the flow depth, with the maximum velocity being greater than the speed of the flow front (Figs. 3 and 5, Kneller *et al*., 1999; Lowe *et al*., 2002; Sher & Woods, 2015). Consequently, material from the back of the flow is advected towards the head (e.g. Sher & Woods, 2015); Gladstone *et al*., (2004) noted in this regard that density stratification in the pre-release fluid leads to preferential advection of lighter fluid towards the flow front. However, previous studies have focused on the case in which flow properties vary monotonically behind the head, and not considered the case in which the longitudinal velocity structure is heterogeneous, i.e., when multiple pulses are initiated separately in time but eventually merge distally from source, resulting in cyclic waxing-waning velocity structure in the flow dynamics.

Here advection is visualized by separating both single- and multi-pulsed flows into primary and secondary components, corresponding to the front and back of the flow at initiation (Fig. 3). In the single-pulsed flow, the second component essentially moved with the fluid immediately in front, and quicker than the current head velocity. In the multi-pulse flows, the internal fluid velocity of the second pulse exceeded both that of the fluid pulse immediately preceding it and of the current head velocity (Fig. 6 and section 4.2), resulting in the forward advection of the second pulse being accelerated compared to that of the second flow component in the single-pulsed flows. The tracked advection rates of the second pulse in multi-pulsed flows were 10% larger than the internal flow front visualized in the single-pulsed flows, i.e., c 0.11 ms^{-1} *vs.* 0.10 ms^{-1} (Fig. 4). The increase in internal advection may in part be attributed to the additional momentum generated by the second lock-gate release. Effectively, in multi-pulse system the second flow component is restrained by the second lock gate, against gravity, for longer than in the single-pulse experiments. Thus, the delay between two releases creates a greater pressure difference in the multi-pulse system than that in the single-pulse system, due to the difference in the height of dense fluid in the two lock boxes.

By the time of the second lock gate release, the enhanced pressure gradient results in the formation of an internal wave and thus an increase in internal advection rates in the multi-pulse system.

Furthermore, in the multi-pulse system, the second pulse is released into the stratified remnant of the primary pulse. Stratification of the primary pulse is driven by entrainment of ambient fluid into the primary pulse after it has been released. The secondary pulse therefore forms and propagates on a neutrally buoyant level, in a similar fashion to intrusions in stratified quiescent fluids (Britter & Simpson, 1981; de Rooij *et al*., 1999; Bolster *et al*., 2008) but here modulated by the background velocity field of the primary pulse. As mixing induced stratification gradually decreases density of the primary pulse towards the density of the ambient, and as the secondary pulse is denser than the ambient, the secondary pulse will be confined within the primary pulse. If the secondary pulse is denser then the primary pulse the intrusion will occur along the lower boundary of the flow. A consequence is that the second pulse will experience reduced drag as its interaction with the solid lower and upper flow-ambient fluid boundary is limited, i.e. lower and upper interface shear-stress (Härtel et al., 2000) is reduced in comparison to single, or the primary component of multi-pulse flows (Fig. 8).

Given that internal fluid velocity in the body of a gravity current is always greater than the head velocity (Kneller *et al*., 1999; Lowe *et al*., 2002; Sher & Woods, 2015), once a following pulse has begun to interact with the velocity field of the first pulse, the second pulse must eventually be advected towards the flow front. Therefore, it is concluded that the intrusion of the second pulse and the merging of two pulses seen in the experiments is an inevitable consequence of the interaction between pulses within dilute multi-pulsed density flows.

4.2. Conceptual models of deposition from multi-pulsed flows

Since the flow dynamics of multi-pulsed flows vary along the flow pathway differently to those of single-pulsed flows, the spatial evolution of their deposits is expected to be distinguishable. Given that upward-fining and upward-coarsening grading patterns suggest deposition from waning and waxing turbidity currents, respectively (Kneller & Branney, 1995; Hand, 1997; Mulder *et al*., 2003; Amy *et al.*, 2005; Basilici *et al.*, 2012), the waxing-waning phenomenon within multi-pulsed flows should lead to the deposition of inverse graded intervals corresponding the passage of a pulse (assuming the flow remains depositional and that an appropriate range of grain sizes is available for transport). In addition, the grading patterns of multi-pulse turbidites likely vary from proximal to distal regions, due to the progressive advection of pulses towards the flow front with increasing run-out distance. This advection should result in a progressive reduction in the time between pulses, decreasing to zero at the point of merging with the flow head; where multiple pulses are present, some may amalgamate before this point. Hence, in any associated turbidite deposit, an original pulsing signal might be relatively accurately preserved proximally, such that the relative spacing between inverse to normal grading cycles is representative of the timing differences between pulses at initiation. The signal might then be progressively distorted up to the point of merging, expressed in reductions in the relative vertical spacing of inverse to normal grading cycles and also in a reduction in the number of such cycles present. The signal will eventually be lost once all pulse components of the flow have completely merged. It should be noted that the relative spacing between cycles will also be dependent on the sedimentation rate.

Figure 9 shows the likely links between a range of turbidity current types, as defined by their longitudinal velocity structures, and their associated turbidite deposits. The deposits are based upon usage in, e.g. Bouma (1962), Lowe (1982) and Gutiérrez-Pastor *et al*., (2013) and references therein. Thus single turbidites with normal grading are deposited by single-pulsed turbidity currents (Fig. 9A). Stacked turbidites represent the closed vertically juxtaposed deposits of two or more such flows (Fig. 9B); the close spacing is taken to imply short inter-flow time durations. Amalgamated turbidites (Fig. 9C) are compound deposits of two (or more) flows in which the later flow eroded into the deposits of the earlier flows. Pulsed turbidites (Fig. 9D) are the deposits of multi-pulsed flows whose individual pulses have interacted; depending on the cause of the pulsing, during early pulse interaction (e.g. Fig. 9D-i) each deposition interval may be similar to a single turbidite, but without any evidence that might indicate a period of flow inactivity between each one (e.g. turbidite mud or hemipelagite). When the pulses have significantly interacted (e.g. Fig. 9D-ii) the time separation between them, and thus the vertical separation of cycles in the deposit, will be reduced. Note: the terms pulsed and stacked turbidites are used here regardless of the originating mechanism of the pulses or whether pulses have distinct mineralogical character.

The initial delay times between different pulses in a multi-pulsed flow depend on the flow generation mechanisms. For a flow initiated by a series of retrogressive submarine landslides, each pulse can be linked to a discrete slumping episode and thus the delay times between individual pulses are controlled by the timing between successive failures. This timing may relate to the natural rate of slope instability propagation, but for a flow initiated by a single large multi-pulsed earthquake or by closely spaced initial shocks and aftershocks (e.g. Goldfinger *et al.*, 2012), the delay times may relate to the spacing between different components of the seismic shock. When a multi-pulsed flow is formed by the combination at channel confluences of different single-pulsed turbidity flows, which were initially triggered synchronously in different channel heads, the delay time between pulses depends on the arrival time differences of the individual flows at the confluence (which depend in turn on channel lengths and intra channel flow velocities). The implications for deposit interpretation for each of these formation mechanisms are considered below.

The depositional structure of flows initiated by retrogressive slope failures (whether seismically generated or not) is shown in Fig. 10A. If there is no initial interaction between the two single-pulsed flows, stacked turbidites could be expected to form proximally. If the flows start to interact, the second flow would behave as a second pulse in a combined flow, and would thus be advected progressively towards the front of that flow. The vertical depositional structure would transition along the flow pathway from having a stacked to multi-pulsed character, finally becoming uni-pulsed (or single-pulsed) after the point of pulse merging. When initially distinct flows combine at confluences, the longitudinal variation in the vertical grading structure of associated turbidites is expected to be similar to that postulated in Fig. 10A, but with an additional pulsing character acquired at the point of combination. In Fig. 10B a case is shown in which flows are triggered synchronously in each of three channels C1, C2 and C3 but take different times to reach their first downstream confluence. This 3D model is extrapolated from the 2D experimental configuration. The actual deposit character will vary depending on the magnitude of each pulse and the nature of the setting. For example, a bi-pulsed flow is shown forming at the C1-C2 confluence, and persisting to from C1-C2 to C3 confluence, where it merges with the flow in C3 to make a tri-pulsed flow that eventually evolves into a uni-pulsed flow. However, had the constituent pulses of the flow formed at the C1-C2 confluence already merged before the C1-C2 to C3 confluence, uni-pulsed flows in channels C1-C2 and C3 would have combined to make a bi-pulsed flow, depositing a bi-pulsed turbidite immediately downstream, and a uni-pulsed turbidite more distally. If the delay times between flows were sufficiently long to prevent their interaction single turbidites would be deposited in each of channels C1, C2 and C3, two stacked turbidites would be deposited downstream of the C1-C2 confluence and three downstream of the C1-C2 to C3 confluence. In complex natural settings, multi-pulsed turbidity currents can be generated by both retrogressive slumping, with pulse timing either dictated by the timing of seismic shaking or by unforced slope failure processes, and by flow combination at confluences of flows that may or may not have a primary pulsed character.

It should be noted that the depositional models proposed in Fig. 10 disregard the effects of flow bypassing (e.g. Stevenson *et al*., 2013; Talling, 2013) or erosion and of local topography features (Eggenhuisen *et al*., 2010). Were bypassing or erosion to occur during flow run-out, some parts of the vertical grading profiles described in the figure might be partially or fully absent, with concomitant increases in deposit thicknesses further downstream.

4.3. Seismo-turbidites

Earthquake-triggered turbidites are commonly deposited along large, active tectonic margins such as Cascadia and Sumatra (Goldfiner *et al*., 2007; St-Onge *et al*., 2012). The deposits of flows generated in this way are called ""seismo-turbidites" (*sensu* Shiki *et al.*, 2000, and references therein). Here the potential application of the conceptual models described above is investigated, both to refine models of flow evolution and to suggest new interpretational options. Sumner *et al*. (2013) document drop-core – derived records of Holocene turbidites deposited on the southwest Sumatra margin, and consider whether they were seismically triggered. Of interest here are turbidites with complex grading patterns, such as those recovered from the updip 4MC and downdip 2MC locations (Fig. 11A). At the 4MC location a succession of three turbidite units without intervening hemiplegic sediments have a deposition motif that could be interpreted either as stacked turbidites (separate events, Fig.

9B), the interpretation favoured by Sumner et al. (2013), or as a tri-pulsed turbidite (one event, Fig. 9D), deposited by a single, pulsed, seismically-generated turbidity current. The sequence of deposits at 2MC appears to comprise one thick basal turbidite and two much thinner overlying turbidites (Sumner *et al*., 2013); the overall upward-fining grading profile of the basal 2MC turbidite suggests that it is the deposit of a single-pulse flow (e.g. Fig. 10A). Sumner *et al*., (2013) did not correlate the 2MC deposit to other turbidites found locally in the system such as those at 4MC. Although this interpretation may correctly reflect that the 4MC and 2MC locations did not lie on the same fairway, an alternative explanation now permitted by the work detailed here is that the 4MC tri-pulsed turbidite and the uni-pulsed 2MC turbidite could represent the deposits of a single flow that was tri-pulsed at 4MC but evolved via pulse merging to be uni-pulsed at 2MC (Fig. 10). In this interpretation, the pattern of ground shaking that initiated flow might be distinguishable in the deposits at 4MC, but have been shredded at 2MC.

Cascadia channel is the channel that extends downstream from the confluence of the Juan de Fuca and Willapa channels (Fig. 11B; Goldfinger *et al*., 2016). Core-based studies of Holocene sediments suggest that great earthquake shocks/aftershocks commonly result in the deposition of multi-pulsed turbidites in the Cascadia Basin (Goldfinger *et al*., 2007; Gutiérrez-Pastor *et al*., 2013). For example, where the same number of turbidites are found in each of the tributary channels and downstream of confluence of a linked channel system, it can be inferred that seismic events synchronously triggered turbidity currents in each of the tributaries, such that turbidity currents combined at confluences (Goldfinger *et al.*, 2012). Thus, should the number of coarse-grained sediment intervals within a correlated bed increase downstream of a confluence, the extra pulses were likely generated by a flow combination mechanism similar to that outlined in Fig. 10B. Figure 11B provides an example of such an increase, in which the “T3” bi-pulsed turbidite found at the 12PC location in the upstream Juan de Fuca channel is correlated with a tri-pulsed T3 at the 25PC location in the downstream Cascadia channel. The thickest interval of coarse sediments at 25PC is attributed to a single pulse flow component derived from the Willapa channel that mixed with a bi-pulsed flow from the Juan de Fuca channel (Fig. 11B; Gutiérrez-Pastor *et al*., (2013). Gutiérrez-Pastor *et al*., (2013), Goldfinger *et al.,* (2008), Goldfinger *et al*., (2012) and Patton *et al*., (2015) recognize that the pattern of pulsing seen in the majority of Holocene and late

Pleistocene turbidites correlated along the Cascadia margin appears to be consistent within each deposit. They interpret the multi-pulsed character of these beds to indicate flow initiation by the large magnitude (M>9) seismic events that characterize this margin. In this interpretation the apparent spatial persistence of pulsing character is contrary to the expectation of pulse merging described above. Either the pulses arise another way, the pulse merging phenomenon observed at laboratory scale does not occur within larger scale turbidity currents, or the merging length scale in such natural settings is longer that the spacing of sample locations. Further work is required to assess these possible explanations.

5. CONCLUSIONS

Physical modelling of multi-pulsed, solute density flows suggest that under most circumstances individual pulses within such flows must be advected forwards through the flow until they merge with the flow head. In natural dilute particulate gravity currents (turbidity currents), such pulsing flow structure may be acquired at flow initiation and be represented in any deposits by an interval of inverse grading (i.e., upwards coarsening) for each pulse. Assuming that such pulses are progressively advected towards the flow front with natural turbidity currents, a progressive reduction in the time between pulses is expected in progressively more distal locations, eventually decreasing to zero when the pulse merges with the flow head. Therefore an original pulsing signal might be relatively accurately preserved proximally, become progressively distorted up to the point of merging where the signal is completely lost ("signal shredded"). This may explain why normal grading is the predominant turbidite grading style in distal locations. Pulsing flow character may also arise when synchronously triggered flows combine at confluences; forward pulse advection will also progressively distort then shred pulses of this character. In natural settings, such as the Cascadia margin, the development of flow pulsing has already been inferred from the grading patterns within turbidites deposited downstream of confluences. The possibility that multi-pulsed flows may evolve spatially to become uni-pulsed can be invoked in studies of turbidites deposited on the southwest Sumatra margin, and permits a wider range of potential correlations to be considered. The multi-pulsed saline flows presented in this paper show that pulse merging is effectively inevitable whilst interacting primary and secondary pulses remain active. Given that waning flows suggest upward fining deposition and waxing flows suggest the opposite, the extrapolation to predict the depositional patterns of pulsed turbidites appears reasonable. Nevertheless, the extrapolation should ideally be supported by experimental models of sediment-bearing flows together with a scaling analysis to more robustly link the characteristic lengths of pulse merging at laboratory scale and those at natural system scale; both are the subject of ongoing work.

ACKNOWLEDGEMENTS

This study was funded by Turbidites Research Group (sponsors: Anadarko, BG, BP, ConocoPhillips, Dana, ENI, Nexen, OMV, Petronas, Shell, Statoil, Tullow, Woodside). All authors have no conflict of interest to declare. We would like to thank Robert Thomas and Helena Brown in the Sorby Environmental Fluid Dynamics Laboratory, University of Leeds for their assistance with the experiments. We would also like to thank Associate Editor J. Baas, reviewers C. Goldfinger, S. Southern and an anonymous reviewer for their constructive comments on an earlier version of this paper.

REFERENCES

Amy, L. A., Talling, P. J., Peakall, J., Wynn, R. B. and **Arzola Thynne, R. G.** (2005) Bed geometry used to test recognition criteria of turbidites and (sandy) debrites. *Sed. Geol.*, **179**, 163–174.

Baas, J. H., Haughton, P. D. W. and **Choux, C.** (2005) Coupling between suspended sediment distribution and turbulence structure in a laboratory turbidity current. *J. Geophys. Res.*, **110**, doi:10.1029/2004JC002668.

Basilici, G., de Luca, P. H. V. and **Poiré, D. G.** (2012) Hummocky cross-stratification-like structures and combined-flow ripples in the Punta Negra Formation (Lower-Middle Devonian, Argentine Precordillera): A turbiditic deep-water or storm-dominated prodelta inner-shelf system? *Sed. Geol.*, **267–268**, 73–92.

Best, J. L., Kostaschuk, R. A., Peakall, J., Villard, P. V. and **Franklin, M.** (2005) Whole flow field dynamics and velocity pulsing within natural sediment-laden underflows. *Geology*, **33(10)**, 765–768.

Bonnecaze, R. T., Huppert, H. E. and **Lister, J. R.** (1993) Particle-driven gravity currents. *J. Fluid Mech.,* **250**, 339–369.

Bolster, D., Hang, A. and **Linden, P. F.** (2008) The front speed of intrusion into a continuously stratified medium. *J. Fluid Mech*., **594**, 369-377.

Bouma, A.H. (1962) Sedimentology of some Flysch Deposits: A Graphic Approach to Facies Interpretation. Elsevier, Amsterdam, 168 pp.

Brand, A., Noss, C., Dinkel, C. and **Holzner, M.** (2016) High-resolution measurements of turbulent flow close to the sediment-water interface using a bistatic acoustic profiler. *Journal of Atmospheric and Oceanic Technology*, **33**, 769–788.

Britter, R. E. and **Simpson, J. E.** (1978) Experiments on the dynamics of a gravity current head. *J. Fluid Mech.,* **88**, 223–240.

Britter, R. E. and **Simpson, J. E.** (1981) A note on the structure of the head of an intrusive gravity current. *J. Fluid Mech.,* **112**, 459–466.

Bull, S., Cartwright, J. and **Huuse, M.** (2009) A subsurface evacuation model for submarine slope failure. *Basin Res.*, **21**, 433–443.

Canals, M., Lastras, G., Urgeles, R., Casamor, J. L., Mienert, J., Cattaneo, A., De Batist, M., Haflidason, H., Imbo, Y., Laberg, J. S., Locat, J., Long, D., Longva, O., Masson, D. G., Sultan, N., Trincardi, F. and **Bryn, P.** (2004) Slope failure dynamics and impacts from seafloor and shallow sub-seafloor geophysical data: Case studies from the COSTA project. *Mar. Geol.*, **213**, 9–72.

Craig, R. G. A., Loadman, C., Clement, B., Rusello, P. J. and **Siegel, E.** (2011) Characterization and testing of a new bistatic profiling acoustic doppler velocimeter: The Vectrino-II.

Proceedings of the IEEE/OES/CWTM *Tenth Working Conference on Current Measurement Technology*, Monterey, CA, 246–252.

de Rooij, F., Linden, P. F. and **Dalziel, S. B.** (1999) Saline and particle-driven interfacial intrusions. *J. Fluid Mech.*, **389**, 303-334.

Di Federico, V., Cintoli, S. and **Bizzarri, G.** (2006) Viscous spreading of non-Newtonian gravity currents in radial geometry. *WIT Transactions on Engineering Sciences*, **52**, 399–408.

Dorrell, R. M., Peakall, J., Sumner, E. J., Parsons, D. R., Darby, S. E., Wynn, R. B., Özsoy, E. and **Tezcan, D.** (2016) Flow dynamics and mixing processes in hydraulic jump arrays: Implications for channel-lobe transition zones. *Mar. Geol.*, **381**, 181–193.

Eggenhuisen, J. T., McCaffrey, W. D., Haughton, P. D. W. and **Butler, R. W. H.** (2010) Small-scale spatial variability in turbidity-current flow controlled by roughness resulting from substrate erosion: field evidence for a feedback mechanism. *J. Sed. Res.*, **80**, 129-136.

GebCO (2014) http://www.gebco.net/data_and_products/gridded_bathymetry_data/

Gladstone, C., Ritchie, L. J., **Sparks, R. S. J.** and **Woods, A. W.** (2004) An experimental investigation of density-stratified inertial gravity currents. *Sedimentology*, **51**, 767-789.

Goldfinger, C., Galer, S., Beeson, J., Hamilton, T., Black, B., Romsos, C., Patton, J., Nelson C. H., Hausmann, R. and **Morey, A.** (2016) The importance of site selection, sediment supply, and hydrodynamics: A case study of submarine paleoseismology on the northern Cascadia margin, Washington USA. *Mar. Sed.*, (2016). https://doi.org/10.1016/j.margeo.2016.06.008

Goldfinger, C., Grijalva, K., Bürgmann, R., Morey, A.E., Johnson, J.E., Nelson, C.H., Gutiérrez-Pastor, J., Ericsson, A., Karabanov, E., Chaytor, J.D., Patton, J. and **Gràcia, E.** (2008) Late Holocene rupture of the northern San Andreas fault and possible stress linkage to the Cascadia subduction zone. *Earth Bulletin of the Seismological Society of America*, **98(2)**, 861–889.

Goldfinger, C., Morey, A. E., Nelson, C. H., Gutiérrez-Pastor, J., Johnson, J. E., Karabanov, E., Chaytor, J. and **Eriksson, A.** (2007) Rupture lengths and temporal history of significant earthquakes on the offshore and north coast segments of the Northern San Andreas Fault based on turbidite stratigraphy. *Earth Planet. Sci. Lett.*, **254**, 9–27.

Goldfinger, C., Nelson, C.H., Morey, A.E., Johnson, J.E., Patton, J., Karabanov, E., Gutiérrez-Pastor, J., Eriksson, A.T., Gràcia, E., Dunhill, G., Enkin, R.J., Dallimore, A. and **Vallier, T.** (2012) Turbidite event history—methods and implications for Holocene paleoseismicity of the Cascadia subduction zone. U.S. Geological Survey Professional Paper 1661-F, 170p. (Available free at http://pubs.usgs.gov/pp/pp1661f/).

Gutiérrez-Pastor, J., Nelson, C. H., Goldfinger, C. and **Escutia, C.** (2013) Sedimentology of seismo-turbidites off the Cascadia and northern California active tectonic continental margins, northwest Pacific Ocean. *Mar. Geol.*, **336**, 99–119.

Hallworth, M. A., Huppert, H. E., Phillips, J. C. and **Sparks, R. S. J**. (1996) Entrainment into two-dimensional and axisymmetric turbulent gravity currents. *J. Fluid Mech.*, **308**, 289–311.

Hand, B. M. (1997) Inverse grading resulting from coarse-sediment transport lag. *J. Sed. Res.*, **67(1)**, 124-129.

Härtel, C., Meiburg, E. and **Necker, F.** (2000) Analysis and direct numerical simulation of the flow at a gravity current head. Part 1. Flow topology and front speed for slip and no-slip boundaries. *J. Fluid Mech.*, **418**, 189–212.

Haughton, P. D. W. (1994) Deposits of deflected and ponded turbidity currents, Sorbas Basin, Southeast Spain. *J. Sed. Res., Section A: Sedimentary Petrology and Processes*, **64(2)**, 233-246.

Hogg, A., Nasr-Azadani, M., Ungarish, M. and **Meiburg, E.** (2016) Sustain gravity currents in channel. *J. Fluid Mech.*, **798**, 853-888.

Holyer, J. Y. and **Huppert, H. E.** (1980) Gravity currents entering a two- layer fluid. *J. Fluid Mech.*, **100(4),** 739–767.

Hughes, G. O. (2016) Inside the head and tail of a turbulent gravity current. *J. Fluid Mech.*, **790**, 1–4.

Huppert, B. H. E. (1998) Quantitative modelling of granular suspension flows. *Philosophical Transactions of the Royal Society A: Mathematical, Physical and Engineering Sciences*, ***356***, 2471–2496.

Huppert, H. E. (1982) Propagation of two-dimensional and axisymmetric viscous gravity currents over a rigid horizontal surface. *J. Fluid Mech.*, **121**, 43–58.

Huppert, H. E. (2006) Gravity currents: A personal perspective. *J. Fluid Mech.*, **554**, 299–322.

Huppert, H. E. and **Simpson, J. E.** (1980) The slumping of gravity currents. *J. Fluid Mech.*, **99(4)**, 785–799.

Islam, M. A. and **Imran, J.** (2010) Vertical structure of continuous release saline and turbidity currents. *J. Geophys. Res.*, **115**, 1-14, doi:10.1029/2009JC005365.

Ismail, H., Viparelli, E. and **Imran, J**. (2016) Confluence of density currents over an erodible bed. *J. Geophys. Res.: Earth Surface*, **121**, 1251–1272.

Jerolmack, D. J. and **Paola, C.** (2010) Shredding of environmental signals by sediment transport. *Geophys. Res. Lett.*, **37(19)**, 1–5.

Johnson, C. G. and **Hogg, A. J.** (2013) Entraining gravity currents. *J. Fluid Mech*, **731**, 477–508.

Kneller, B. and **Buckee,** C. (2000) The structure and fluid mechanics of turbidity currents: a review of some recent studies and their geological implications. *Sedimentology*, **47**, 62–94.

Kneller, B. and **McCaffrey, W. D.** (2003) The interpretation of vertical sequences in turbidite beds: the influence of longitudinal flow. *J. Sed. Res.*, **73(5)**, 706–713.

Kneller, B. C. and **Branney, M. J.** (1995) Sustained High-Density Turbidity Currents and the Deposition of Thick Massive Sands. *Sedimentology*, **42**, 607–616.

Kneller, B. C., Bennett, S. J. and **McCaffrey, W. D**. (1999) Velocity structure, turbulence and fluid stresses in experimental gravity currents. *J. Geophys. Res.*, **104(C3)**, 5381.

Lowe, D.R. (1982) Sediment gravity flows; II, Depositional models with special reference to the deposits of high-density turbidity currents. *J. Sed. Petrol.*, **52(1)**, 279-297.

Lowe, R. J., Linden, P. F. and **Rottman, J. W.** (2002) A laboratory study of the velocity structure in an intrusive gravity current. *J. Fluid Mech.*, **456**, 33–48.

MacVicar, B. J., Dilling, S., Lacey, R. W. J. and **Hipel, K.** (2014) A quality analysis of the Vectrino II instrument using a new open-source MATLAB toolbox and 2D ARMA models to detect and replace spikes. In: Schleiss AJ, de Cesare G, Franca MJ, Pfister M, (eds.), *River Flow 2014, CRC Press/Balkema*: Leiden; 1951–1959.

Middleton, G. V. (1966) Experiments on density and turbidity currents II. *Can. J. Earth Sci.*, **3**, 523–546.

Middleton, G. V. (1993) Sediment deposition from turbidity currents. *Annu. Rev. Earth Planet. Sci.*, **21**, 89–114.

Mikada, H., Mitsuzawa, K., Matsumoto, H., Watanabe, T., Morita, S., Otsuka, R., Sugioka, H., Baba, T., Araki, E. and **Suyehiro, K.** (2006) New discoveries in dynamics of an M8 earthquake-phenomena and their implications from the 2003 Tokachi-oki earthquake using a long term monitoring cabled observatory. *Tectonophysics*, **426(1–2)**, 95–105.

Mulder, T. and **Alexander, J.** (2001) The physical character of subaqueous sedimentary density flow and their deposits. *Sedimentology*, **48(2)**, 269–299.

Mulder, T. and **Alexander, J.** (2001) The physical character of subaqueous sedimentary density flow and their deposits. *Sedimentology*, **48(2)**, 269–299.

Mulder, T., Syvitski, J. P. M., Migeon, S., Faugères, J. C. and **Savoye, B.** (2003) Marine hyperpycnal flows: Initiation, behaviorand related deposits. A review. *Mar. Petrol. Geol.*, **20**, 861–882.

Nakajima, T. and **Kanai, Y.** (2000) Sedimentary features of seismoturbidites triggered by the 1983 and older historical earthquakes in the eastern margin of the Japan Sea. *Sed. Geol.*, **135**, 1-19.

Paola, C., Straub, K., Mohrig, D. and **Reinhardt, L.** (2009) The ‘unreasonable effectiveness’ of stratigraphic and geometric experiments. *Earth-Sci. Rev.*, **97**, 1-43.

Patton, J.R., Goldfinger, C., Morey, A.E., Ikehara, K., Romsos, C., Stoner, J., Djadjadi- hardja, Y., Udrekh, Ardhyastuti, S., Gaffar, E.Z. and **Vizcaino, A.** (2015) A 6600 year earthquake history in the region of the 2004 Sumatra-Andaman sub- duction zone earthquake. *Geosphere*, **11**, 2067–2129, doi:10.1130/GES01066.1.

Piper, D. J. W. and **Normark, W. R.** (2009) Processes That Initiate Turbidity Currents and Their Influence on Turbidites: A Marine Geology Perspective. *J. Sed. Res.*, **79**, 347–362.

Piper, D. J. W., Cochonat, P. and **Morrison, M. L.** (1999) The sequence of events around the epicentre of the 1929 GrandBanks earthquake: initiation of debris flows and turbidity current inferred from sidescan sonar. *Sedimentology*, **46**, 79–97.

Piper, D. J. W., Shor, A. N. and **Clarke, J. E. H.** (1988) The 1929 “Grand Banks” earthquake, slump, and turbidity current. *Geol. Soc. Am. Spec. Pap.,* **229**, 77–92.

Rottman, J. W. and **Simpson, J. E**. (1983) Gravity currents produced by instantaneous releases of a heavy fluid in a rectangular channel. *J. Fluid Mech.*, **135**, 95–110.

Sequeiros, O. E. (2012) Estimating turbidity current conditions from channel morphology: A Froude number approach. *J. Geophys. Res.: Oceans*, **117(4)**, 1–19.

Sher, D. and **Woods, A. W.** (2015) Gravity currents: entrainment, stratification and self-similarity. *J. Fluid Mech.*, **784**, 130–162.

Shiki, T., Cita, M. and **Gorsline, D.** (2000) Sedimentary features of seismites, seismo-turbidites and tsunamiites—an introduction. *Sed. Geol.*, **135**, vii–ix.

Simpson, J. E. (1982) Gravity currents in the laboratory, atmosphere, and ocean. *Annu. Rev. Fluid Mech.*, **14**, 213–234.

Stevenson, C. J., Talling, P. J., Wynn, R. B., Masson, D. G., Hunt, J. E., Frenz, M., Akhmetzhanhov, A. and **Cronin, B. T.** (2013) The flows that left no trace: Very large-volume turbidity currents that bypassed sediment through submarine channels without eroding the sea floor. *Mar. Petrol. Geol.*, **41**, 186–205.

St-Onge, G., Chapron, E., Mulsow, S., Salas, M., Viel, M., Debret, M., Foucher, A., Mulder, T., Winiarski, T. and **Desmet, M.** (2012) Comparison of earthquake-triggered turbidites from the Saguenay (Eastern Canada) and Reloncavi (Chilean margin) Fjords: implications for paleoseismicity and sedimentology. *Sed. Geol.*, **243**, 89-107.

Sumner, E. J. and **Paull, C. K.** (2014) Swept away by a turbidity current in Mendocino submarine canyon, California. *Geophys. Res. Lett.*, **41(21)**, 7611–7618.

Sumner, E. J., Siti, M. I., McNeill, L. C., Talling, P. J., Henstock, T. J., Wynn, R. B., Djajadihardja, Y. S. and **Permana, H.** (2013) Can turbidites be used to reconstruct a paleoearthquake record for the central Sumatran margin? *Geology*, **41(7)**, 763–766.

Talling, P. J. (2013) Hybrid submarine flows comprising turbidity current and cohesive debris flow: Deposits, theoretical and experimental analyses, and generalized models. *Geosphere*, **9(3)**, 460–488.

Talling, P. J., Allin, J., Armitage, D. A., Arnott, R. W. C., Cartigny, M. J. B., Clare, M. A., Felletti, F., Covault, J. A., Girardclos, S., Hansen, E., Hill, P. R., Hiscott, R. N., Hogg, A. J., Clarke, J. H., Jobe, Z. R., Malgesini, G., Mozzato, A., Naruse, H., Parkinson, S., Peel, F. J., Piper, D. J. W., Pope, E., Postma, M., Rowley, P., Sguazzini, A., Stevenson, C. J., Sumner, E. J., Sylvester, Z., Watts, C. and **Xu, J.** (2015) Key Future Directions for Research on Turbidity Currents and Their Deposits. *J. Sed. Res.*, **85**, 153–169.

Xu, J. P., Noble, M. A. and **Rosenfeld, L. K.** (2004) In-situ measurements of velocity structure within turbidity currents. *Geophys. Res. Lett.*, **31(9)**, 1-4.

FIGURE CAPTIONS

Fig. 1: Schematic sedimentary log of a turbidite with intervals of inversely graded grain size. Inverse grading in pulsed deposits is distinct from basal inverse grading, which can be produced by other mechanisms (e.g. Hand, 1997). Note: S = Silt; VF = very fine sand; F = fine sand; M = medium sand; C = coarse sand; VC = very coarse sand; G = granules. Mudstone clasts and hemipelagites are not always present.

Fig. 2: Schematic of the experimental set up. A 5 m-long flume with two lock boxes (each 0.125m long) set up in series at one end to enable the delayed release of a second pulse to generate a pulsed flow. Two overspill boxes were used to reduce the effect of returning waves associated with slumping of dense fluids in the lock boxes. Acoustic-Doppler Velocimetry (ADV) was used to collect velocity data at successive downstream positions located at 0.365, 0.465, 0.585, 0.675, 0.765, 0.865, 0.965, 1.065, 1.265, 1.465, 1.665 and 1.865 m.

Fig. 3: Photographs of the flow at different time intervals for (A) a single-pulsed flow experiment with 0 second delay time and (B) a multi-pulsed flow experiment with 4 second delay time between two pulses. In (B) the two pulses completed merged between 15s and 18s. Gridlines on the bottom of the flume were used for camera alignment and flow position tracking. Inset shows the advection of the second pulse within the first pulse.

Fig. 4: Plots showing the location of the front of (A) a single-pulsed and (B) a multi-pulsed flow over time. Dashed curves are best fits of front position data collected from multiple experiments.

Fig. 5: Contour plots showing spatio-temporal variation of internal velocity structure within (A) a single-pulsed flow and (B) a multi-pulsed flow at 0.365 m, 0.675 m, 0.865 m, 1.265 m and 1.665 m downstream from the back of the lock box. Red and blue lines between plots indicate the arrivals of the primary and secondary pulses, respectively; these become progressively closer with time in multi-pulsed flows. Note that the low velocity variations that appear as vertical stripes of amplitude (< 0.025 ms-1) show the effect of surface waves, white horizontal stripes in each subplot are areas of no data.

Fig. 6: Contour plots showing spatio-temporal variations of depth-averaged velocity of (A) Single-pulsed flows and (B) Multi-pulsed flows. Note: Dashed and dotted curves are best fits of front positions of primary and secondary pulses respectively.

Fig. 7: Comparison between depth-averaged velocity profiles of single- and multi-pulsed flows at three different downstream positions: (A) Raw data and (B) Filtered data. Note: Raw data were filtered by using Savitzky-Golay smoothening process in MatLab with a polynomial order of three and a framelength of 151.

Fig. 8: Model of multi-pulsed flow propagation based on experimental results. Vertical axis shows flow height (h), horizontal axes show density (d) and velocity (v). Note: The model illustrates the scenario in which the second pulse intrudes into the first pulse at neutrally buoyant level (see text for discussion of alternative scenarios).

Fig. 9: Conceptual models illustrating the depth-averaged velocity-time profile for various turbidity current configurations and their inferred deposits. (A) A single-pulse turbidite with an upward fining grain size profile. (B) Stacked turbidites comprising two single-pulsed turbidities with a presence of Bouma Te (silt or clay layer) in between. (C) Amalgamated turbidite with sharp interface between different inverse-to-normal grading cycles due to the erosion of a latter flow into the deposit of an earlier flow. (D) Pulsed turbidites at relatively proximal and distal locations. Note: 1) the lack of linear correspondence between the time and depth records (shown schematically for Fig. 9A, and implied for 9B-D); 2) pulsed turbidites might have internal erosion surfaces instead of (or in addition to) inverse grading depending on pulse strength.

Fig. 10: Initiation mechanisms of multi-pulsed flows: **(A)** Multi-pulsed flow triggered by retrogressive slope failures and conceptual turbidite patterns for longer vs. shorter failure delays in the left-hand and right-hand panels, respectively and **(B)** Tri-pulsed flow triggered by flow combination at channels, and possible turbidite grading patterns.

Fig. 11: Multi-pulsed turbidites **(A)** offshore Sumatra at the 4MC and 2MC core locations (modified after Sumner *et al*., 2013), dashed curve shows proposed channel conduit and **(B)** in the linked Juan de Fuca and Cascadia channels at the 12PC and 25PC locations (modified from Gutiérrez-Pastor *et al*., 2013), white curve shows channel conduit (Goldfinger *et al*.,

2016). Note: because grainsize was estimated directly from the core, sediments finer than 62 μm cannot be distinguished (A). Magnitude of magnetic data reflect grainsize of turbidites. Bathymetric data were taken from GebCO, 2014.

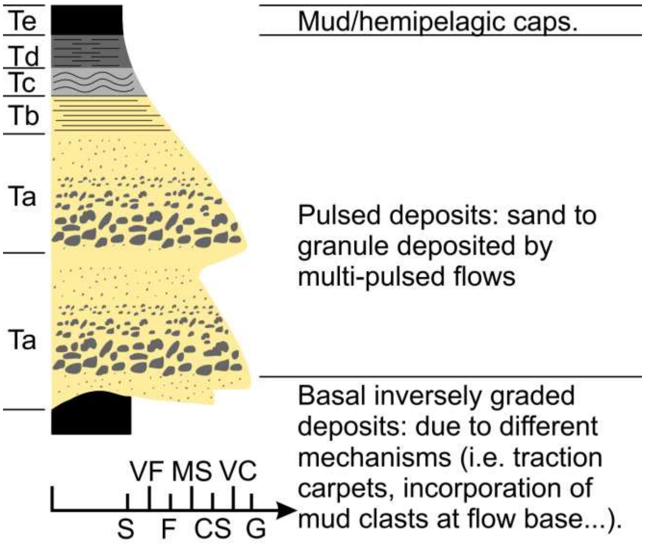

Figure 1

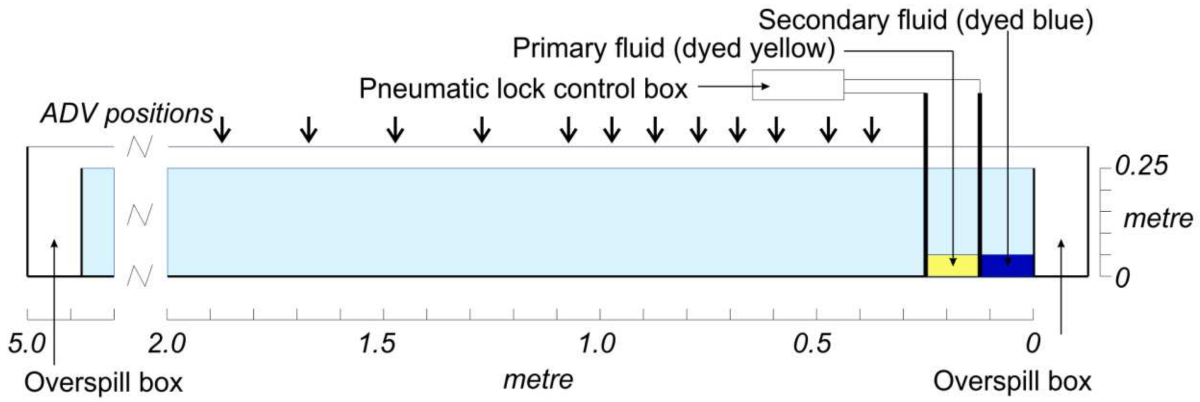

Figure 2

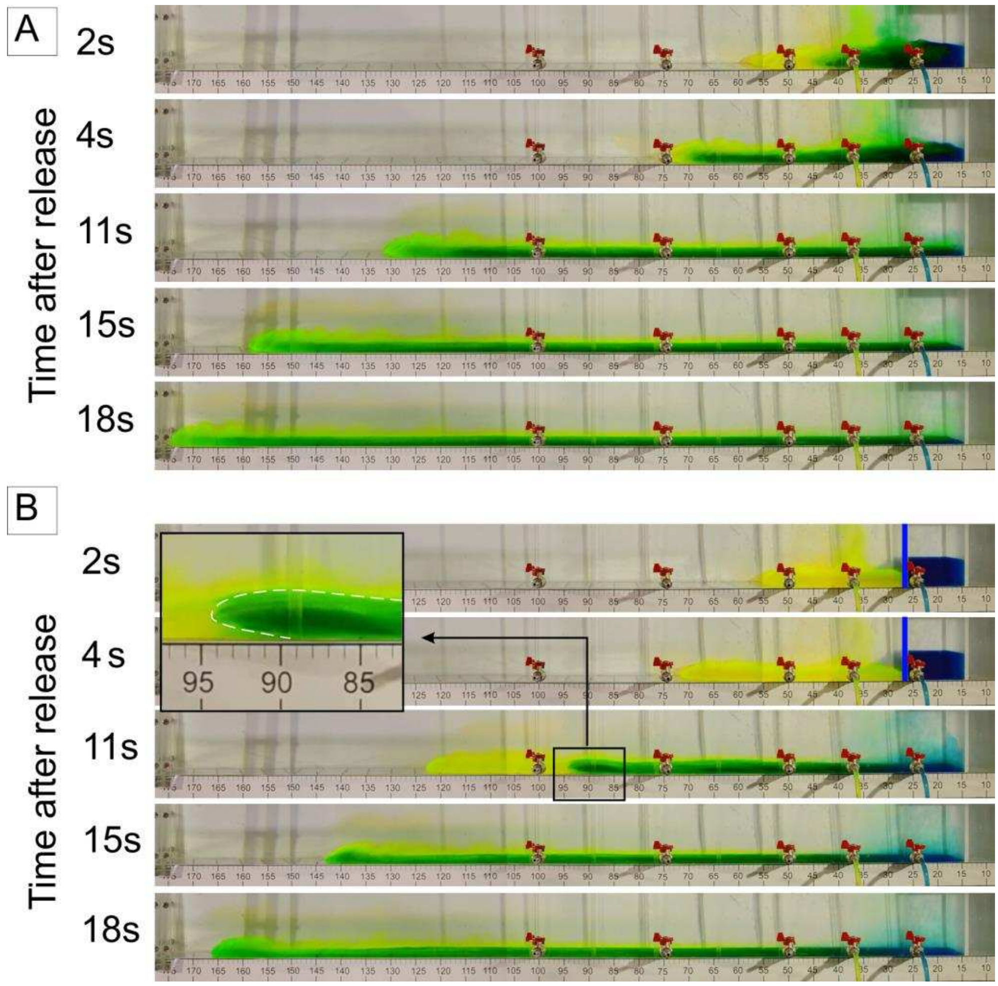

Figure 3

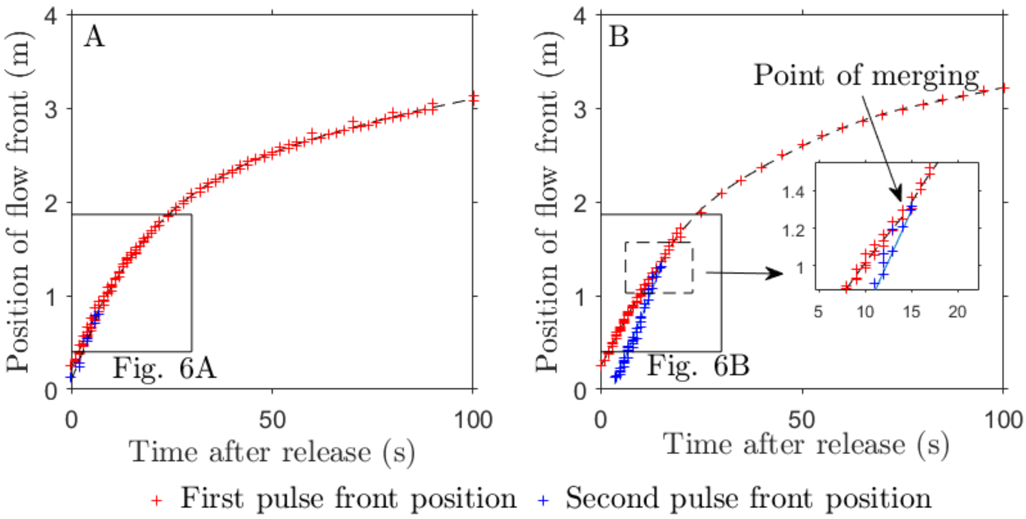

A
B
Position of flow front (m)
Time after release (s)
Fig. 6A
Fig. 6B
Point of merging
First pulse front position
Second pulse front position

Figure 4

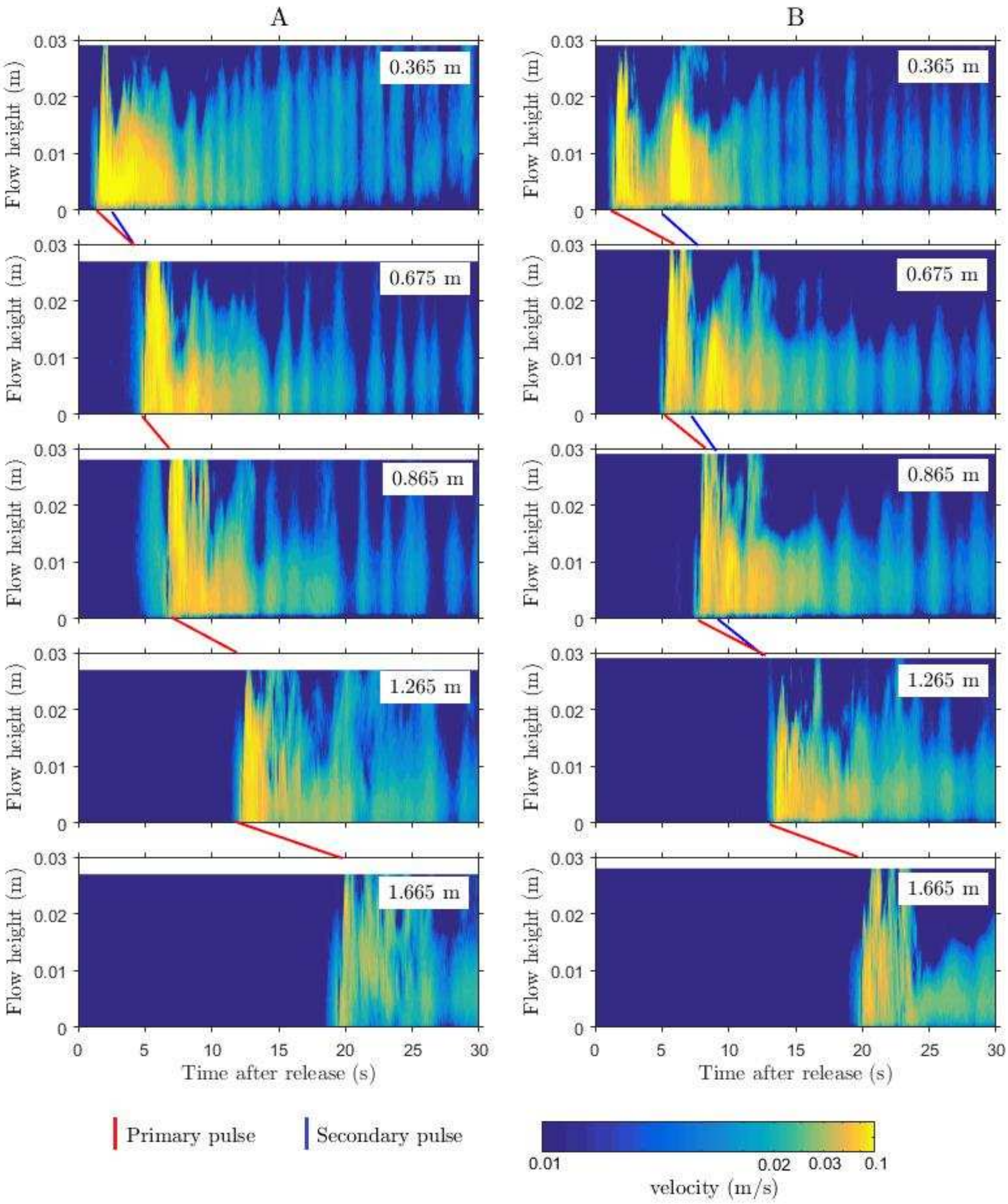
A
B
0.365 m
0.675 m
0.865 m
1.265 m
1.665 m
Flow height (m)
Time after release (s)
Primary pulse
Secondary pulse
velocity (m/s)
0.01
0.02
0.03
0.1

Figure 5

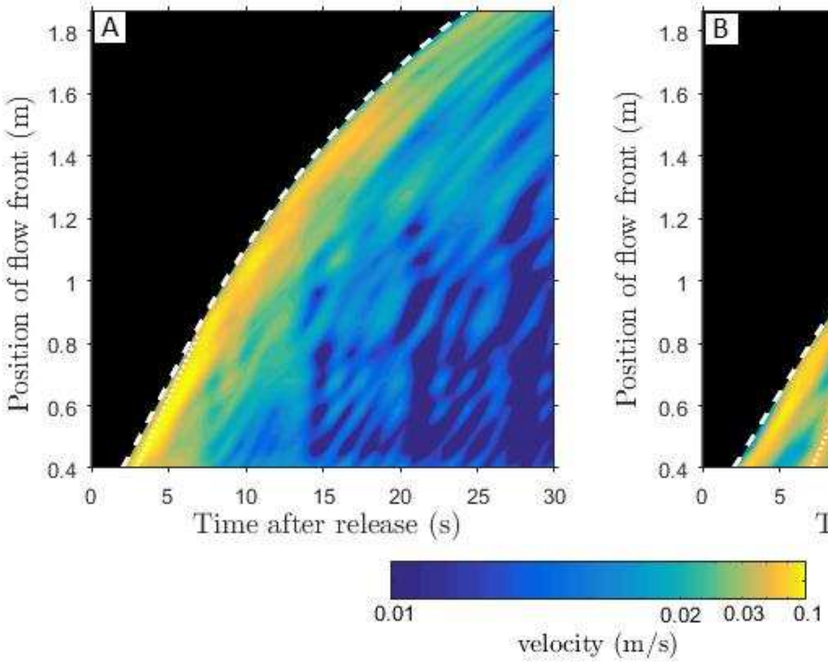

Figure 6

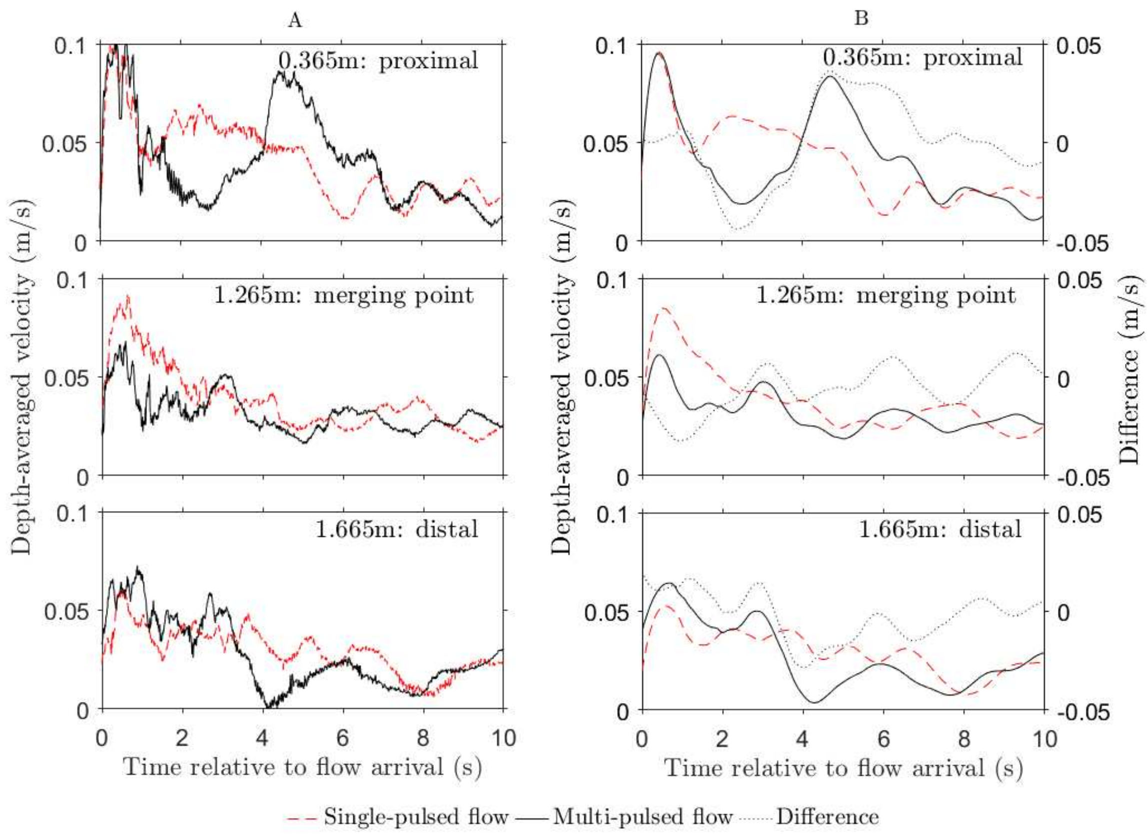

Figure 7

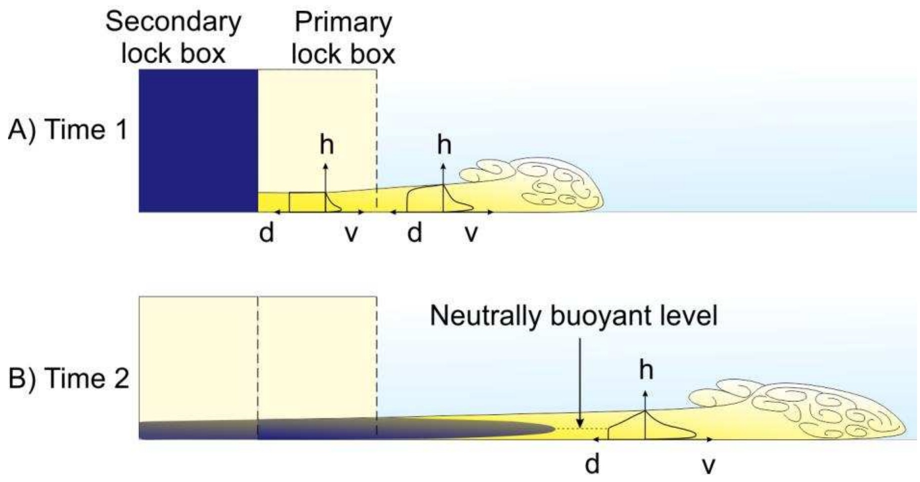
Secondary lock box
Primary lock box
A) Time 1
h
h
d
v
d
v
Neutrally buoyant level
B) Time 2
h
d
v

Figure 8

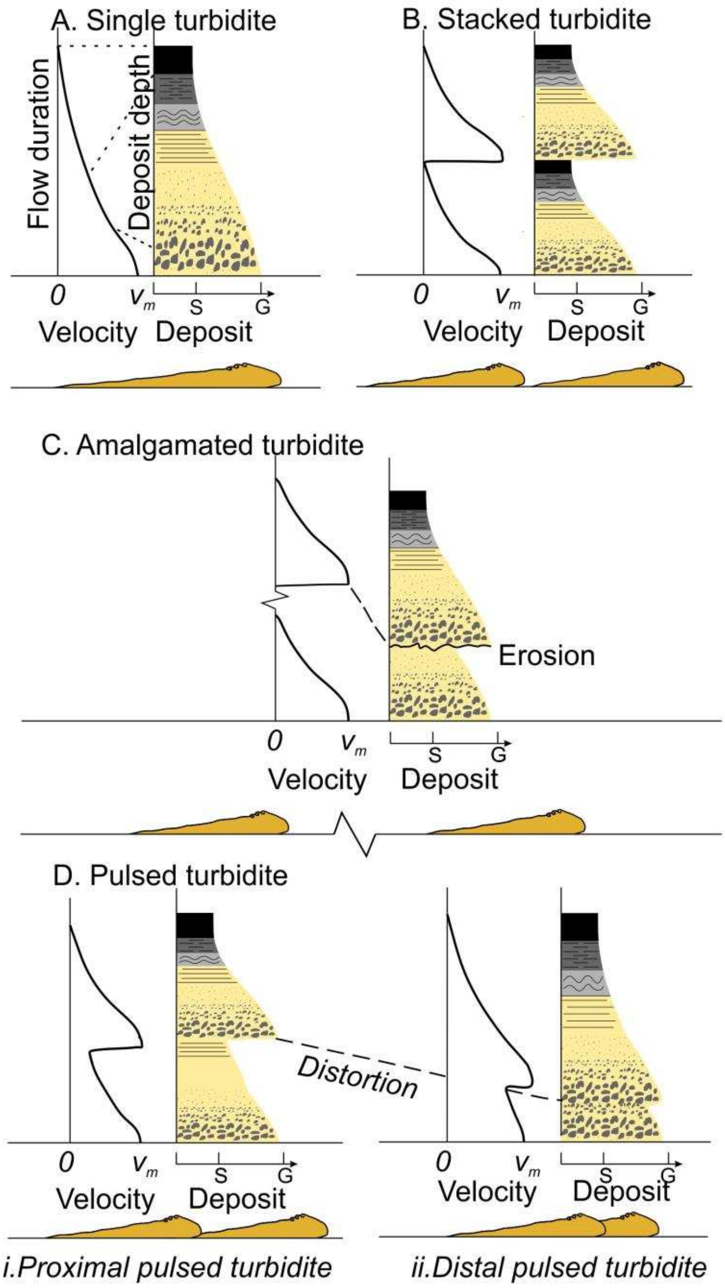
A. Single turbidite
Flow duration
Deposit depth
0
v_m
S
G
Velocity
Deposit
B. Stacked turbidite
0
v_m
S
G
Velocity
Deposit
C. Amalgamated turbidite
Erosion
0
v_m
S
G
Velocity
Deposit
D. Pulsed turbidite
Distortion
0
v_m
S
G
Velocity
Deposit
0
v_m
S
G
Velocity
Deposit
i.Proximal pulsed turbidite
ii.Distal pulsed turbidite

Figure 9

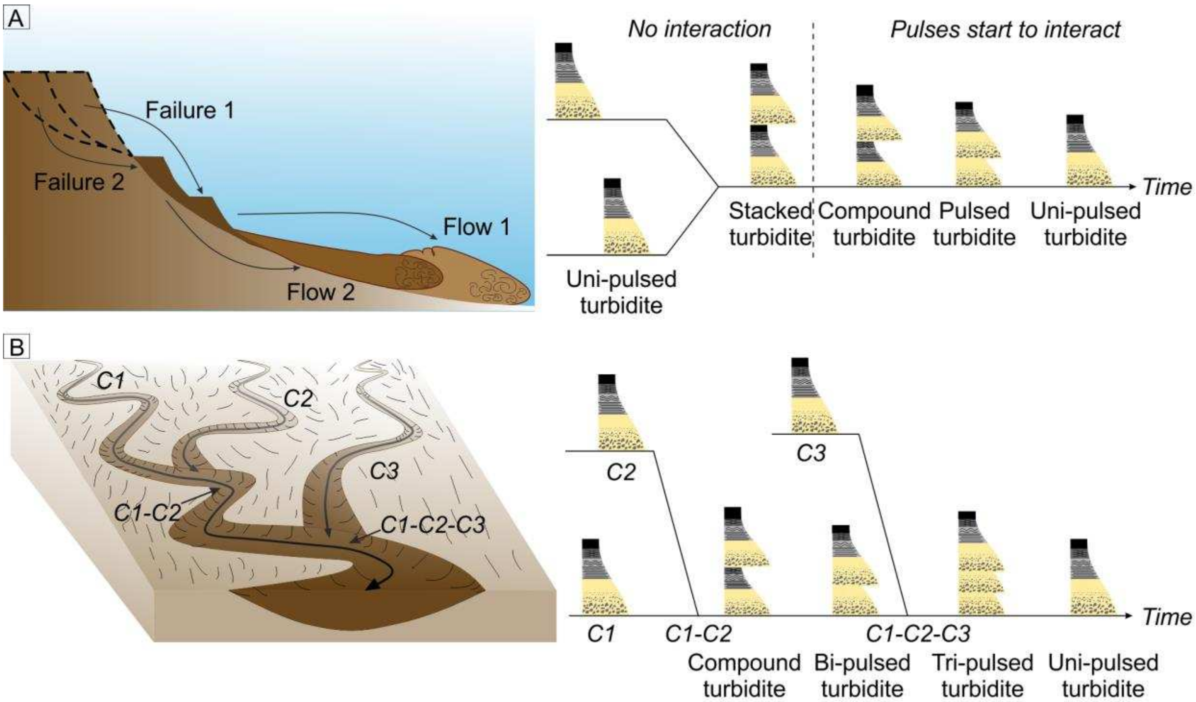

769

770 Figure 10

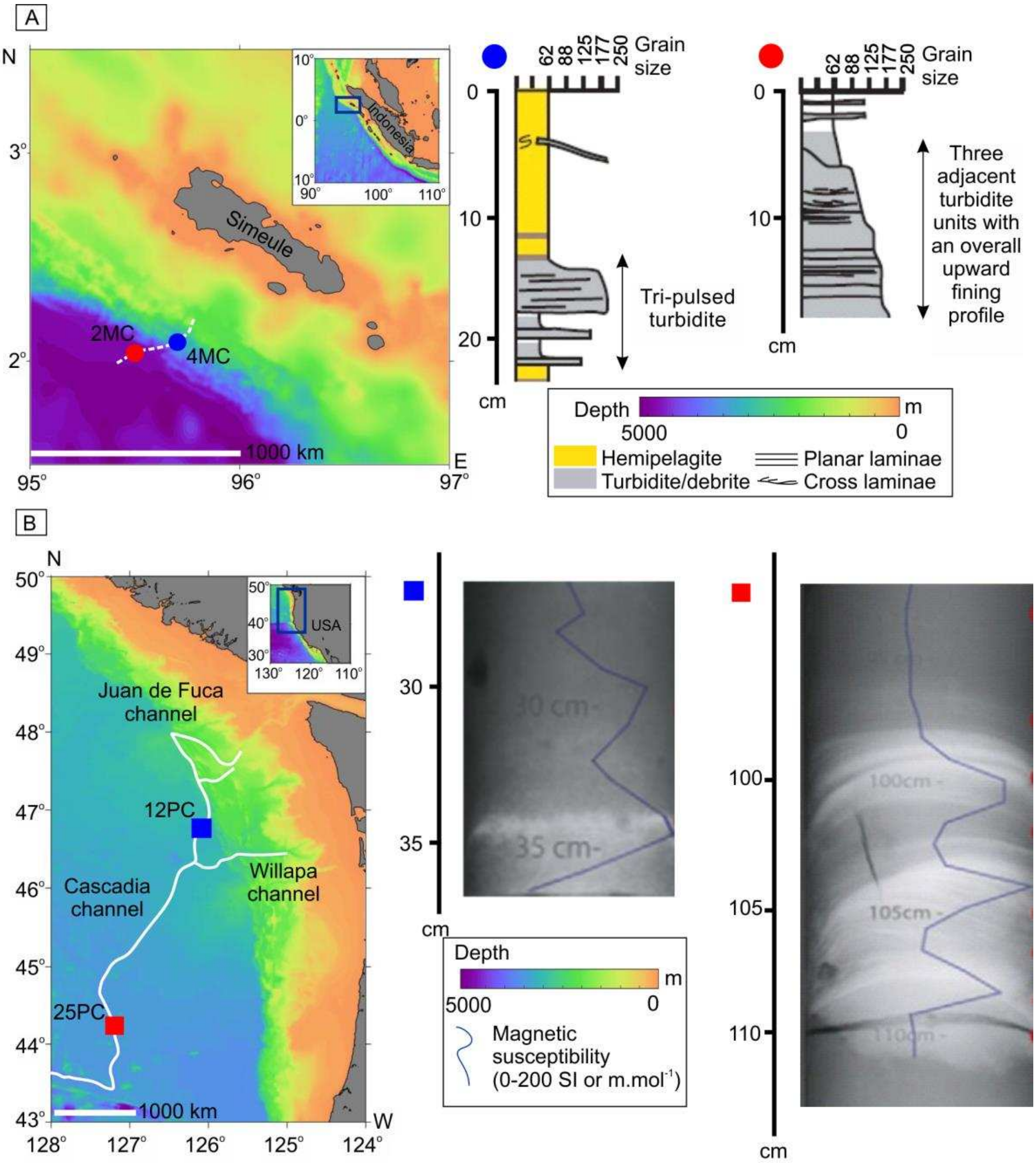
A
N
3°
2°
95°
96°
97°
E
Simeule
2MC
4MC
1000 km
10°
0°
10°
90°
100°
110°
Indonesia
Grain size
62 88 125 177 250
0
10
20
cm
Tri-pulsed turbidite
Three adjacent turbidite units with an overall upward fining profile
Depth
m
5000
0
Hemipelagite
Turbidite/debrite
Planar laminae
Cross laminae
B
N
50°
49°
48°
47°
46°
45°
44°
43°
128°
127°
126°
125°
124°
W
Juan de Fuca channel
12PC
Cascadia channel
Willapa channel
25PC
1000 km
USA
130°
120°
110°
30
35
30 cm
35 cm
100
105
110
100cm
105cm
Magnetic susceptibility (0-200 SI or m.mol⁻¹)

Figure 11